PHILOSOPHICAL MAGAZINE
2020, VOL. 100, NO. 9, 1102–1128
https://doi.org/10.1080/14786435.2020.1725680

Taylor & Francis
Taylor & Francis Group

PART A: MATERIALS SCIENCE

Geometric dynamic recrystallization of austenitic stainless steel through linear plane-strain machining

Yaakov Idell [a,b], Jörg Wiezorek[b], Giovanni Facco[b], Andreas Kulovits[b] and M. Ravi Shankar[c]

[a]Materials Science Division, Lawrence Livermore National Laboratory, Livermore, CA, USA; [b]Department of Mechanical Engineering and Materials Science, University of Pittsburgh, Pittsburgh, PA, USA; [c]Department of Industrial Engineering, University of Pittsburgh, Pittsburgh, PA, USA

ABSTRACT

Type 316L austenitic stainless steel was severely plastically deformed at room temperature using linear plane-strain machining in a single pass that imparted shear strains up to 2.2 at strain rates up to 2×10^3 s^{-1}. The resulting microstructures exhibited significant grain size refinement and improved mechanical strength where geometric dynamic recrystallization was identified as the primary microstructural recrystallization mechanism active at high strain rates. This mechanism is rarely observed in low to medium stacking fault energy materials. The critical stress required for twin initiation is raised by the combined effects of refined grain size and the increase in stacking fault energy due to the adiabatic heating of the chip, thus permitting geometric dynamic recrystallization. The suppression of martensite formation was observed and is correlated to the significant adiabatic heating and mechanical stabilisation of the austenitic stainless steel. A gradient of the amount of strain induced martensite formed from the surface towards the interior of the chip. As the strain rate is increased from 4×10^2 s^{-1}–2×10^3 s^{-1}, a grain morphology change was observed from a population of grains with a high fraction of irregular shaped grains to one dominated by elongated grain shapes with a microstructure characterised by an enhanced density of intragranular sub-cell structure, serrated grain boundaries, and no observable twins. As strain rates were increased, the combination of reduction in strain induced martensite and non-uniform intragranular strain led to grain softening where a Hall-Petch relationship was observed with a negative strengthening coefficient of −0.08 MPa $m^{1/2}$.

ARTICLE HISTORY
Received 19 November 2019
Accepted 22 January 2020

KEYWORDS
Nanocrystalline; 316L stainless steel; severe plastic deformation; microstructure; mechanical properties; dynamic recrystallization

1. Introduction

316L austenitic stainless steel is a widely used structural material in biomedical, petrochemical, and nuclear power related applications due to its superior

CONTACT Yaakov Idell idell1@llnl.gov Materials Science Division, Lawrence Livermore National Laboratory, Livermore, CA, USA; Department of Mechanical Engineering and Materials Science, University of Pittsburgh, 634 Benedum Hall, 3700 O'Hara Street, Pittsburgh, PA 15261, USA

corrosion and thermomechanical properties [1]. The relatively low yield strength of austenitic stainless steels like 316L, when compared to other structural materials, is considered a weakness that is typically addressed by strengthening through cold work via strain hardening and/or strain-induced martensite (SIM) formation. The formation of SIM yield strength and work hardening [2], and nanocrystalline SIM has been reported to enhance fatigue resistance [3]. Unfortunately, the SIM also possesses deleterious effects in austenitic steels, such as reduced ductility, toughness, and corrosion resistance [4]. SIM is produced when the austenitic stainless steel is deformed at temperatures below the composition-dependent martensite start temperature, M_d [5,6], which is typically below room temperature [7]. An alternative route to improve strength while limiting SIM is significant grain refinement through severe plastic deformation (SPD) processing techniques such as equal channel angular pressing (ECAP), high-pressure torsion (HPT), and surface mechanical attrition treatment (SMAT) [8–14]. SPD of metals and alloys can result in grain refinements to the ultrafine grained, 0.1 μm < D_{grain} < 1.0 μm, and the nanocrystalline, D_{grain} < 0.1 μm, size regimes [11–13,15,16]. Recently, 316L austenitic stainless steel has been surface processed with a nearly SIM-free chip characterised by an ultrafine grained and nanocrystalline grain size through the application of linear plane-strain machining [17].

Linear plane-strain machining is a surface plastic deformation process that is capable of imparting large strains in excess of unity. In the this technique, shown schematically in Figure 1, a sharp wedge-shaped tool removes a preset depth of material (a_o) via motion perpendicular to its cutting edge in a single pass at room temperature [18]. This results in the formation of a severely plastically deformed

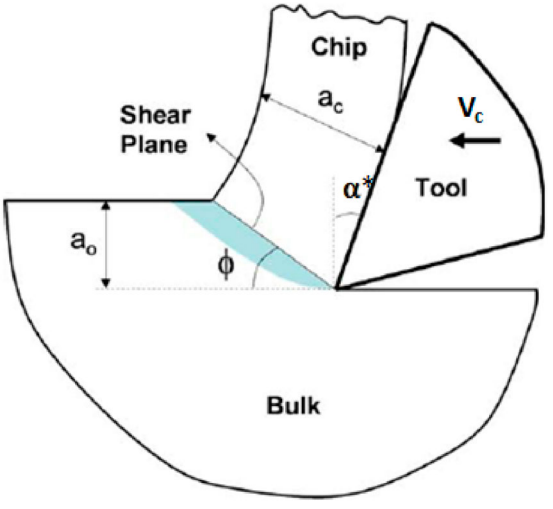

Figure 1. Schematic of linear plane-strain machining where the geometric parameters are shown. The shear plane angle (ϕ) along with the rake angle (α^*) will determine the average shear strain and magnitude of the deformation field [18].

chip. The effective magnitude of the plastic deformation that occurs both in compression and in shear is dependent on the cutting speed (V_c), rake angle (α), material characteristics, and frictional heat produced. Material characteristics that affect the plastic deformation are dependent on strain rate ($\dot{\gamma}$), strain hardening, strength, and heat conductivity [19]. Large rake angle tools have typically shown to produce less overall deformation; meanwhile, small or negative rake angle tools have been shown to produce significant deformation [18,20].

Previous studies of the 316L austenitic stainless steel produced chip from linear plane-straining machining have monitored the microstructural and mechanical property changes at room temperature [17,21]. However, the mechanisms controlling grain size, grain morphology, and SIM formation remain to be elucidated. This paper presents and discusses a thorough microstructural investigation with the aim to identify the mechanisms explaining the different processing-microstructure-property relationships that have been previously observed.

2. Experimental materials and methods

2.1. Linear plane-strain machining of 316L austenitic stainless steel

A custom-built linear machining device, which ensures plane-strain conditions, was used to severely plastically deform a commercially available, cold-rolled, and annealed 316L austenitic stainless steel plate (Table 1). The stainless steel plate was sectioned into 60 mm x 45 mm x 3 mm samples, and processed through linear plane-strain machining by a high strength steel (HSS) tool with a rake angle of $\alpha^* = 0$ °, constant cutting depth of $a_o = 150$ μm, and tool velocities of 2.5, 6.25, 12.5, and 25 cms^{-1} at room temperature. The resultant chip has dimensions of 5 mm to 13 mm (length) x 3 mm (width) x 0.15 mm to 0.21 mm (thickness) where the length and thickness of the chip varies as a function of tool velocity. When the tool velocity is decreased, the chip has a shorter length and slightly increased thickness primarily due to the pile-up caused by the deformation process at the cutting tool leading edge.

2.2. Monitoring of mechanical property and microstructure changes

The microstructural changes and mechanical properties in the 316L austenitic stainless steel linear plane-strain machined chips were monitored through a combination of hardness measurements, vibrating sample magnetometry

Table 1. AISI Standard Composition for 316L austenitic stainless steel (weight percent).

C	Mn	*P*	S	Si	Cr	Ni	Mo	N	Fe
0.03	2.00	0.045	0.03	0.75	16.00–18.00	10.00–14.00	2.00–3.00	0.1	BAL

(VSM) measurements, X-ray diffraction (XRD), transmission electron microscopy (TEM), and infrared (IR) thermography. The experiments were performed with the Leco M-400-G Vickers hardness testing machine using a load of 50 g and a dwell time of 10 s, Lakeshore vibrating sample magnetometer model 7404 operated with a maximum magnetic field of 21.7 kOe (2.17 T) at 298 K, Bruker D8 Discover x-ray diffractometer operated at 40 kV and 40 mA with copper K-alpha radiation (λ = 0.15406 nm) that was fitted with the LYNXEYE detector in a symmetric Bragg–Brentano setup over a 2θ scan range between 40 ° to 85 °, FLIR A325sc IR camera operated at 60 frames per second, and the JEOL JEM200CX and JEM2100F transmission electron microscopes (TEM) operated at 200 kV, which were equipped with the NanoMEGAS (Digistar/ASTAR) precession electron diffraction-assisted automated crystal orientation mapping (PED-ACOM) system with a precession angle was set to 0.7 ° and a step size of 5 nm providing information regarding crystallographic texture, grain orientation, grain shape, and local deformation structure at a nanometer scale spatial resolution [22]. Due to the elongated morphology of the polycrystalline microstructures, the grain sizes were determined from TEM PED-ACOM data by measuring both the major and minor axes of the grains, and then averaging these values. Samples for the TEM experiments were prepared by mechanical thinning of produced chips to ≈ 75 μm thick, punching out of 3 mm diameter discs, followed by electro-polishing using an electrolyte solution of 73% ethanol, 10% butyl cellosolve, 8% perchloric acid, and 9% water at 298 K and 35 V using a Fischione Model 140 twin-jet electro-polisher. The peak fitting software, Fityk [23], was used to fit the peaks of the X-ray diffraction data for deconvolution of overlapping peaks and extraction of quantitative information regarding the microstructure.

3. Results and discussion

3.1. Inverse Hall-Petch relationship

The effective shear strain (γ) and shear strain rates ($\dot{\gamma}$) imposed on the chips by the linear plane-strain machining can be estimated through Equations (2) and (3) [24,25] by determining the permanent shape changes in the chips.

$$\tan\phi = \frac{\frac{a_o}{a_c}\cos(\alpha*)}{1 - \frac{a_o}{a_c}\sin(\alpha*)} \tag{1}$$

Where the shear angle (ϕ) is calculated from a measurement of a_o, a_c (deformed chip thickness), and rake angle (α^*) [25].

$$\gamma = \frac{\cos(\alpha^*)}{\sin(\phi)\cos(\phi - \alpha^*)} \tag{2}$$

$$\dot{\gamma} = \frac{\gamma}{a_o} v_c \cos\phi \tag{3}$$

Table 2 shows the calculated γ and the $\dot{\gamma}$ for the range of tool velocities utilised here. The γ was determined to be relatively insensitive to the tool velocity with values ranging from 2.1–2.2 for all the tool velocities; whereas, the $\dot{\gamma}$ was observed to rapidly increase from $\approx 2 \times 10^2$ s^{-1} to $\approx 2 \times 10^3$ s^{-1} as a function of tool velocity. The measured γ values can be comparable to other SPD techniques such as HPT, SMAT, and ECAP depending on the processing conditions, which have confined geometries or cannot be performed in a single pass at room temperature; however, the $\dot{\gamma}$ from linear plane-strain machining is significantly higher than values previously observed in conventional cold deformation processes or SPD techniques [26,27].

The as received material exhibits a Vickers microhardness of 159 VHN (corresponding to 520 MPa tensile strength). After plane strain machining at the various tool velocities, the microhardness increased significantly, as tabulated in Table 2, to a hardness between ≈ 500 VHN and ≈ 520 VHN. 316L austenitic stainless steel has been previously reported to follow the Hall-Petch relationship with a strengthening coefficient of 0.25 MPa $m^{1/2}$ [13,28]. However, the linear plane-strain machined chips do not follow the Hall-Petch relationship with the same strengthening coefficient. Using the average grain size as measured by XRD (Table 2), the strengthening coefficient is determined to be −0.08 MPa $m^{1/2}$, which indicates that the chips resulting from linear plane-strain machining follow an inverse Hall-Petch relationship. Typically, the hardness of a material increases with decreasing grain size until a critical grain size is attained, generally below 100 nm [29,30], when hardness begins to decrease with decreasing grain size. Below the critical grain size for a given material, the mechanism controlling grain size strengthening is altered as dislocation pile-ups cannot effectively form [31] resulting in grain softening. Coble creep [32,33], grain boundary sliding [34,35], and grain boundary triple junction activity

Table 2. Summary of selected microstructural metrics and properties of 316L austenitic stainless steel of the as received condition and the various tool velocity processed chips.

	As Received	2.5 cms^{-1}	6.25 cms^{-1}	12.5 cms^{-1}	25 cms^{-1}
Average Shear Strain	-	2.2 ± 0.07	2.2 ± 0.08	2.1 ± 0.07	2.1 ± 0.06
Strain Rate (s^{-1})	-	200 ± 2	400 ± 5	800 ± 20	2000 ± 20
Austenite Lattice Parameter (Å)	3.607 ± 0.001	3.5943 ± 0.003	3.5993 ± 0.003	3.5981 ± 0.005	3.5993 ± 0.002
Microstrain (με)	-	0.005 ± 0.002	0.005 ± 0.002	0.006 ± 0.003	0.003 ± 0.002
Stress (GPa)	-	1.323 ± 0.200	1.504 ± 0.200	1.252 ± 0.200	1.323 ± 0.200
Grain Size (nm) – XRD	≈ 20000	≈ 70	≈ 50	≈ 45	≈ 45
Grain Size (nm) – Dark Field TEM	≈ 20000	73 ± 23	45 +/- 7	43 ± 5	50 ± 3
Hardness (VHN)	159	524 ± 18	517 ± 29	498 ± 10	501 ± 12
Tensile Strength (MPa)	≈ 520	≈ 1710	≈ 1690	≈ 1630	≈ 1630
$T_{calculated}$ (°C)	-	106	152	193	253
$T_{experimental}$ (°C)	-	77.9	-	125.4	197.3

[36] have been proposed to account for the plastic deformation without dislocation glide activity and the decrease in flow stress with a decreasing grain size. Based on the inverse Hall-Petch relationship, the grain size strengthening contribution to the tensile strength is calculated to between ≈ 1630 MPa to ≈ 1710MPa as a function of tool velocity, which is equivalent to ≈ 17% to ≈ 23% of the total tensile strength as measured by the microhardness based on average grain size. The remaining 77% to 83% of the total tensile strength can be attributed presumably to other strengthening mechanisms, including contributions from martensite phase fraction, texture, and stored strain for instance.

3.2. Processing-microstructural-property relationships

Figure 2 compares XRD scans of the linear plane-strain machined chips at the various velocities with the as received 316L austenitic stainless steel. The as received material exhibits both high-intensity face-centered cubic (FCC) peaks associated with the austenite phase and low-intensity body-centered cubic peaks associated with the martensite phase. Due to the close proximity of the {110} peak of the martensite phase and {111} peak of the austenite phase, it is necessary to perform peak deconvolution, which permits lattice parameter determination using the Nelson-Riley function for highly accurate and precise values [37] of the austenite (γ-phase) as shown in Table 2. There is a significant compressive shift in the lattice parameter between the as received material and the linear plane-strain machined chips. The lattice parameter appears to be insensitive to tool velocity indicating the direct relationship between the shear strain and residual stresses imparted into the chips. Significant peak broadening is observed in all tool velocity conditions, which can be attributed to grain size reduction and stored microstrain [38]. Using a Williamson-Hall plot to separate

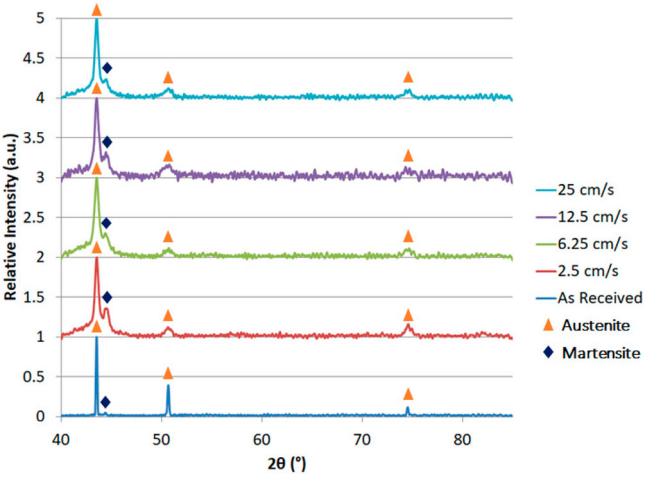

Figure 2. XRD scans of the as-received material and the chips of the various tool velocities where a reduction of the martensite peak is observed as function of tool velocity.

the peak broadening caused by non-uniform microstrain and grain size reduction [39], it was determined that 12% to 20% of the peak broadening stems from grain size reduction as a function of tool velocity, which provides excellent agreement with the hardness measurements. With the peak broadening due to grain size reduction identified, the grain size was determined using Scherrer's Equation [40]. Grain size was determined to range from 70 nm to 45 nm and decreased as a function of increasing tool velocity. The non-uniform microstrain stored in the lattice of the 316L chips accounted for between 80% to 88% of the peak broadening with the corresponding stored microstrain ranging in magnitude from 0.003–0.006 (Table 2). For the specimens obtained with the 2.5, 6.25, and 12.5 cms^{-1} tool velocities, the stored microstrain is consistent with a magnitude of ≈ 0.005 (Table 2). However, for the 25 cms^{-1} tool velocity machining condition the stored microstrain of the resulting 316L chips shows a significant decrease to magnitudes of 0.003. For the highest straining rates attained for the highest tool velocity of 25 cms^{-1}, the thermo-mechanical induced mechanisms activated in the 316L microstructure appears to permit significant strain relief. The significant reduction in the stored microstrain observed for the highest strain rate condition linear plane strain machining indicates a change in the microstructural response of the 316L.

The magnitudes of the observed refinement in grain size, peak broadening, storage of non-uniform microstrain in the lattice, and lattice parameter shift measured by XRD for the plane-strain machining deformed chips are similar to those previously reported for interstitial-free steel [27] and 316L austenitic stainless steel [26] after SPD by ECAP. For the various tool velocity conditions, there are observable changes in the relative XRD peak intensities associated with the {111}, {200} and {220} of austenite, i.e. I_{111}/I_{200} and I_{111}/I_{220}, and an increase in the intensity of the I_{110} peak of the martensite. The changes in the austenite XRD peak intensity ratios, i.e. I_{111}/I_{200} and $I_{111}/I_{220,}$ are consistent with a change in texture, and the increase in martensite peak intensity indicates an increase in the volume of SIM, which are both induced by the machining process. Notably, the observed increase in the relative intensity of the martensite peaks is not as large as would be expected for the amount of strain that has been introduced when a comparison is made to SIM fraction produced during plastic deformation under similar conditions by conventional deformation techniques. For instance, in order to attain shear strain of approximately equivalent magnitude to that imparted to the 316L austenitic stainless steel chips by the linear plane-strain machining through conventional cold rolling, it would require a thickness reduction on the order of 82% to 87% at room temperature, which would be expected to induce ≈ 50% by volume of SIM [4]. There are several possible explanations for the suppression of SIM formation during linear plane-strain machining: (i) the strain rates in this deformation process are much higher as compared to conventional cold rolling, which may result in higher adiabatic heating for the higher strain rates and could promote reversion of the SIM

formed; (ii) the XRD scans were sampled from near the centre of the chip, while the deformed chip may exhibit a gradient microstructure where a maximum amount of SIM is formed at the surface with less SIM formed near the centre; (iii) mechanical stabilisation of austenite occurring during the deformation process. The martensitic transformation typically occurs in a diffusion-less process with para-equilibrium, a condition where substitutional solute atoms do not partition between phases during the transitions creating a minimal free energy condition [41]. This transformation can be affected by the mechanical stabilisation of austenite, which is a phenomenon where the interface between martensite and austenite grains contains glissile dislocations whose motion could be slowed down by the defects in the austenite. For sufficiently large plastic strain, the plastic deformation will introduce a high density of geometrically necessary defects in the austenite that can completely prevent movement of the martensite-austenite interfaces to halt the martensite transformation process [42–45].

VSM and quantitative XRD analysis of the SIM provide necessary information to understand the effect of martensite formation on the processing-microstructure-property relationships of the linear plane-strain machined chips. Both complementary martensite volume fraction (MVF) determination techniques are necessary because XRD only reveals surface related information; based on the 2θ range for the relevant austenite and martensite peaks, the detected Cu-kα X-rays will only penetrate between 5 μm to 8 μm into the depth of the 316L chip samples [38]. In contrast, VSM measurements provide bulk sample information; therefore, combining the two measurement techniques will allow probing for the presence of a possible SIM gradient in the 316L chip material. Through XRD, the strain-induced martensite volume fraction can be determined (XRD-MVF) by measuring the phase fraction of the two phases present in 316L austenitic stainless steel, austenite and martensite. This technique is based on the principle that each phase in a mixture, as measured by the total integrated intensity of all diffraction peaks for that phase, is proportional to the volume fraction of that phase [38]. The integrated intensity consists of contributions from both the material scattering factor, R_{hkl}, and instrument factor**.** The material scattering factor is determined by the lattice parameter (ν), multiplicity factor (ρ), temperature factor, absorption factor, Lorentz-Polarization factor, and structure factor, as shown in Equation (4). Cullity [38] describes the relationship between the measured intensities of the martensite (α') and austenite (γ), volume fraction of each phase (C_γ and $C_{\alpha'}$), and the material scattering factors of the two phases in Equation (5). The contributing values to the material scattering are shown in Table 3. The values for the temperature factor, i.e. Debye–Waller factor, B(T), are derived from experimentally determined elemental phonon density of states with an accuracy between 2% to 3% [46]. On the other hand, the instrument factor will be the same for both phases and is based on the XRD beam geometry characteristics,

such as wavelength of the incident beam, radius of the diffractometer, and cross-sectional area of the incident beam. Because the instrument factor is constant for all phases, these contributions will cancel each other out when comparing relative intensities and the intensity ratios for the two phases.

$$R_{hkl} = \left(\frac{1}{v^2}\right)\left[|F_{hkl}|^2 \rho\left(1 + \frac{\cos^2 2\theta}{\sin^2\theta\cos\theta}\right)\right](e^{-2M}) \tag{4}$$

$$\frac{I_\gamma}{I_{\alpha'}} = \frac{R_\gamma C_\gamma}{R_{\alpha'} C_{\alpha'}} \rightarrow C_{\alpha'} = \frac{1}{\left[\frac{I_\gamma R_{\alpha'}}{I_{\alpha'} R_\gamma} + 1\right]} \tag{5}$$

The SIM volume fractions induced by linear plane-strain machining determined here by XRD and VSM are shown in Figure 3. The measured fraction of SIM is insensitive to tool velocity for all velocities above 2.5 cms^{-1}. The VSM measurements show an increase of the SIM volume fraction (VSM-MVF) from the reference state of the as-received materials with a VSM-MVF of ≈ 0.6% to ≈ 3% for the tool velocities of 6.25, 12.5, and 25 cms^{-1}, while a VSM-MVF of ≈ 9% has been determined for the 2.5 cms^{-1} tool velocity. Meanwhile, the XRD-MVF shows an increase to ≈ 15% for tool velocities above 2.5 cms^{-1}, and to ≈ 23% for the 2.5 cms^{-1} tool velocity. The differences between the XRD-MVF and VSM-MVF measurements indicate that a microstructural gradient is developed in the produced chips. The gradient is likely caused by mechanical stabilisation of austenite or adiabatic heating during the linear plane-straining machining.

Table 3. Parameters of the material scattering factor for XRD-MVF determination.

	Austenite	Martensite
Multiplicity Factor [38]	$\{111\}_\gamma$ – 8, $\{200\}_\gamma$ – 6, $\{220\}_\gamma$ – 12	$\{110\}_{\alpha'}$ – 12
Lattice Parameter [37,38]	Measured Values (see Table 2)	2.88 Å
Lorentz-Polarization Factor (based on θ)	$1 + \frac{cos^2 2\theta}{sin^2\theta cos\theta}$	$1 + \frac{cos^2 2\theta}{sin^2\theta cos\theta}$
Temperature Factor (based on B(T) and θ) at 298 K [46]	$B(T) = 0.5853$ Å^2 $M = B(T)s^2$ $s = \frac{\sin\theta}{\lambda}$	$B(T) = 0.3461$ Å^2 $M = B(T)s^2$ $s = \frac{\sin\theta}{\lambda}$
Absorption Factor	Neglected due to independent of θ	Neglected due to independent of θ
Structure Factor (based on θ and constants for atomic form factor from [47])	$F_{hkl} = 4f$ $f(q) = \sum_{i=1}^{4} a_i e^{-b_i q^2} + 4c$ $q = \frac{\sin\theta}{\lambda}$ Where a_1 is 11.7695, b_1 is 4.7611, a_2 is 7.3573, b_2 is 0.3072, a_3 is 3.5222, b_3 is 15.3535, a_4 is 2.3045, b_4 is 76.8805, and c is 1.0369	$F_{hkl} = 2f$ $f(q) = \sum_{i=1}^{4} a_i e^{-b_i q^2} + 4c$ $q = \frac{\sin\theta}{\lambda}$ Where a_1 is 11.7695, b_1 is 4.7611, a_2 is 7.3573, b_2 is 0.3072, a_3 is 3.5222, b_3 is 15.3535, a_4 is 2.3045, b_4 is 76.8805, and c is 1.0369

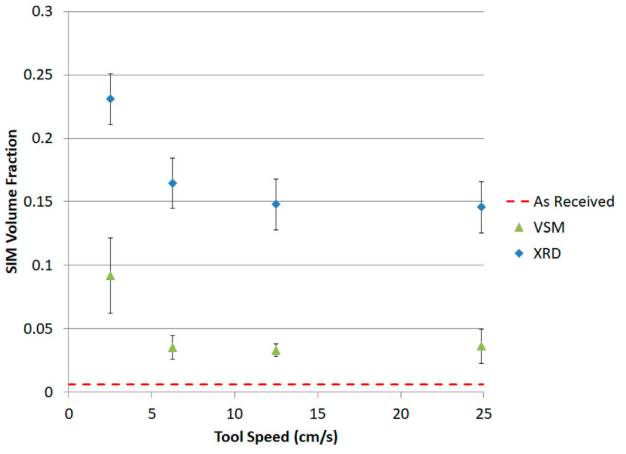

Figure 3. SIM volume fraction of the linear plane-strain machined chip as determined by XRD and VSM revealing suppressed martensite formation and a gradient developed from the surface towards the interior of the chips.

Using data shown in Table 2, the temperature rise in the chip can be estimated theoretically by coupling the work of plastic deformation to the temperature at the shear plane [48].

$$\rho C_p dT = (1\text{-}\beta)\ \sigma(\varepsilon, \dot{\varepsilon}, T)d\varepsilon \tag{6}$$

Equation (6) states that an increase in plastic strain, dε, results in an equivalent increase in temperature, dT. σ(ε,ε̇,T) is the Johnson-Cook model for describing flow stress as a function of strain, ε, strain rate, ε̇, and temperature, T [49] and ρC_p is the product of mass density and heat capacity of 316L austenitic stainless steel. The pre-factor (1-β) is then multiplied by the calculated flow stress. The factor β describes the fraction of the heat transported away from the chip by the bulk material [50], which is determined by:

$$\beta = \frac{1}{4\alpha'}\mathrm{erf}\sqrt{\alpha'} + (1+\alpha')\mathrm{erfc}\sqrt{\alpha'} - \frac{e^{-\alpha'}}{\sqrt{\pi}}\left(\frac{1}{2\sqrt{\alpha'}} + \sqrt{\alpha'}\right) \tag{7}$$

Where α' is a function of the plane-strain machining parameters V_c and a_o, the thermal diffusivity of the bulk material κ, and the shear angle φ [48]:

$$\alpha' = \frac{V_c\ a_o \tan\varphi}{4\kappa} \tag{8}$$

Rearranging the expressions in Equations (6) to (8) determines an estimate for the total temperature rise is determined by the integral [51]:

$$\int_{T_0}^{T_{calc}} \frac{\rho C_p(T)}{1-\left(\frac{T-T_r}{T_m-T_r}\right)^m} dT = (1-\beta)\left(A\varepsilon + \frac{B}{n+1}\varepsilon^{n+1}\right)\left(1 + C\ln\left(\frac{\dot{\varepsilon}}{\dot{\varepsilon}_0}\right)\right) \quad (9)$$

$$C_p(T) = 440.79 + 0.5807T - 0.001T^2 + 7\text{x}10^{-7}T^3 \quad (10)$$

In Equation (9), A (yield strength), B (hardening modulus), C (strain rate sensitivity), $\dot{\varepsilon}_0$, m (thermal softening coefficient) and n (hardening coefficient) are material constants which have been determined through a combination of analytical and empirical techniques [52] to be 305, 441, 0.057, 1, 1.041, and 0.1 for A, B, C, $\dot{\varepsilon}_0$, m, and n respectively. T_r and T_m are the room temperature and material melting temperature, respectively [49].

The temperatures calculated of the different processing conditions using Equation (9) are slightly higher than the temperature rise magnitudes measured by IR-thermography (Table 2). The temperature differences are attributed to required simplifications in the assumptions of the model relative to the conditions and geometries encountered in practice. The Johnson-Cook model assumes an idealised case where all mechanical work that is applied to the chip during deformation will transform to heat; however, the Johnson-Cook model does not account for any heat transfer away from the chip such as conduction or convection. The measured temperature rise from IR-thermography is directly related to the amount of SIM reverted. The temperature rise is shown to be significantly lower for the linear plane strain machining at 2.5 cms^{-1} as compared to the other tool velocity conditions (Table 2). Hence, the chip attained for the slowest velocity machining condition used here, 2.5 cms^{-1}, has appreciably more SIM, which is consistent with the experimental measurements by XRD and

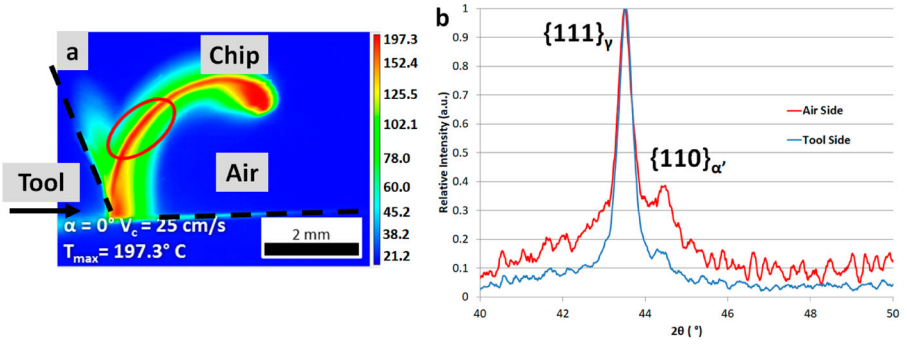

Figure 4. (a) Temperature fields in an IR-thermograph still frame for the 25 cms^{-1} velocity where the dashed lines mark the tool/chip interface and location of the 316L austenitic stainless steel surface, and (b) the associated section of the XRD scan displaying the significant difference in the martensite ($\{110\}_{\alpha'}$) peak intensity when comparing the tool side and the air side of the chip.

VSM. Additionally, the IR-thermography displays a temperature profile across the cross section of the chip. Figure 4a shows that the temperatures from the adiabatic process heating are higher in the central volume regions of the chip than for the surfaces of the chip. For a given chip, the SIM volume fraction is higher at the chip surface where temperatures reach lower maximum values and cooling is more rapid than for the centre of the chip. This establishes SIM reversion conditions for much shorter periods of time at the chip surfaces as compared to the centre of the chip. Therefore, a gradient of the MVF, the SIM formed, is expected to develop in the 316L chip microstructure, increasing from a minimum for the central region to a maximum for the surface region. The adiabatic heating plays an important role and is most likely the primary factor in developing a gradient in the SIM in the chip.

In order to develop a more accurate understanding of the observed gradient in the chips, it is necessary to analyze the surface of both sides of the chips (the previous XRD-MVF measurements were taken near the centre of the chip) as well as the surface of the 316L austenitic stainless steel substrate exposed to the linear plane strain machining pass. Unfortunately for the surface substrate, the XRD-MVF technique is not able to provide reliable data due to significant texturing of the surface; hence, we analyzed the surface substrate using PED-ACOM. The measured volume fraction of SIM through PED-ACOM at the surface substrate of the 316L austenitic stainless steel is $\approx$ 50%, which agrees with the SIM expected for a conventionally cold rolled 316L at similar shear strains [4]. The surface substrate of the 316L austenitic stainless steel is expected to have significantly less imparted strain and adiabatic heating as compared to the produced chips. The reduction in adiabatic heating of the 316L austenitic stainless steel substrate, as clearly observed in Figure 4a, limits the SIM reversion and explains the higher measured volume fraction on the surface substrate as compared to the chips obtained in the linear plane-strain machining operation. For the linear plane-strain machined chips, the side of the chip that was in contact with the surface substrate will be referred to as the 'tool' side of the chip, and the side not in contact with the surface substrate will be referred to as the 'air' side of the chip as shown in Figure 4. The XRD-MVF measurements of the unaltered chips following linear plane-strain machining reveals a SIM volume fraction of $\approx$ 27% to $\approx$ 30% for the air side of the chip and $\approx$ 5% to $\approx$ 12% for the tool side of the chip as function of tool velocity. The observed change in the SIM volume fraction from one side of the chip to the other appears to be driven by the adiabatic heating and cooling. Because the air side of the chip is only in contact with the air, the heat is quickly removed from this side of the chip, which limits its ability to revert the SIM; whereas, the tool side of the chip is at its maximum temperature for longer duration, permitting a higher percentage of SIM reversion. It is hypothesised that the SIM gradient across the chip is controlled by a combination of mechanical stabilisation of the austenite and adiabatic heating.

Bright field (BF) TEM micrographs and their associated selected area diffraction patterns (SADP) of the chips deformed at the various tool velocities are shown in Figure 5. The morphology shows significantly grain refined microstructures with large intragranular defect content for all tool velocities except the 2.5 cms^{-1} tool velocity. Concurently, the respective SADPs are also quite similar for the microstructures of the 316L chips obtained for tool velocity in the range of 6.25 cms^{-1}–25 cms^{-1}. In these microstructures, the grain morphologies become increasing elongated as a function of increasing tool velocity. In contrast, the chip processed for the 2.5 cms^{-1} tool velocity has both relatively large irregular shape grains and smaller more equiaxed grains indicating a bimodal grain size distribution. From the dark field TEM grain size analyses (Table 2), the 6.25, 12.5, and 25 cms^{-1} tool velocities conditions showed similar grain sizes at ≈ 45 nm with a unimodal grain size distribution; meanwhile, the 2.5 cms^{-1} tool velocity condition processing produced a chip microstructure with a significantly larger grain size relative to the other tool velocity machining conditions and a bimodal grain size distribution. The peaks of the bimodal grain size distribution are located at ≈ 40 nm and ≈ 90 nm, respectively, which accounts for the large error in the measurement of the grain size mean. The SADPs obtained for the chips produced by the 6.25, 12.5, and 25 cms^{-1} tool velocity conditions reveal a significant orientation spread with a moderate radial spread, which is consistent with significant grain refinement and moderate levels of non-uniform stored strain. This is consistent with the XRD analysis. The deformation caused by the 2.5 cms^{-1} tool velocity creates a microstructure with a high density of intragranular defect content and refined grains. However, the grains are noticeably larger in the 2.5 cms^{-1} tool velocity condition as compared to those observed in the other tool velocity conditions. The SADP pattern for the 2.5 cms^{-1} tool velocity condition reveals a significantly smaller orientation and larger radial spread as compared to the other

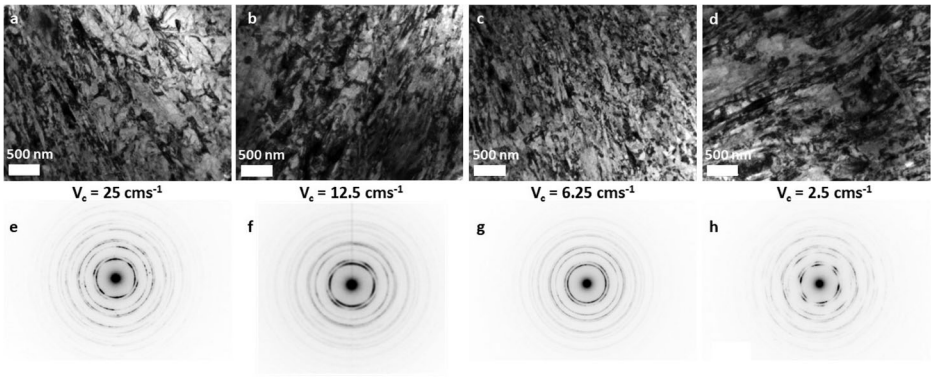

Figure 5. TEM BF micrographs with the associated SADPs for the 4 different tool velocities revealing large defect content and a grain size reduction as a function of the tool velocity. All micrographs and SADPs were taken from the middle of the chips.

higher tool velocity conditions. This indicates more stored strain, a larger average grain size, and smaller average disorientations across grain boundaries. Using the unprocessed SADP for martensite phase fraction analysis, α'-phase, is hindered by the small difference in the inter-planar spacing between the FCC {111} (γ-phase) and the BCC {110} (α'-phase) diffraction rings, i.e. $d_{\{111\}FCC} = 0.206$ nm and $d_{\{110\}BCC} = 0.203$ nm, respectively. The associated respective diffraction rings overlap due to the large radial spread from the stored inhomogeneous strain. For a more quantitative analysis the diffraction rings of the SADP were transformed into an electron diffraction intensity profiles by azimuthal integration, normalisation for the scattering vector length, and applying the pseudo-Voigt function for determining peak shape related parameters through a method termed profile analysis of selected area diffraction (PASAD) [53]. The resulting PASAD data is plotted as the integrated diffracted intensity versus the magnitude of the diffraction vector, which can be interpreted similar to an XRD powder diffractometer scan (Figure 6). For the 6.25, 12.5, and 25 cms^{-1} tool velocities, there is very little SIM as determined by the intensities of the α'-phase related BCC peaks; thus, it is concluded that the majority of the radial spread observed in the SADP is related to non-uniform stored strain. For these three tool velocity conditions the resulting microstructures exhibit similar peak intensities related to the SIM. This is consistent with the XRD-MVF and VSM-MVF results where equivalent SIM volume fraction trends are observed. The radial spread is measured to increase as the tool velocity increases up to 12.5 cms^{-1}, while it decreases for the 25 cms^{-1} tool velocity; thus, the non-uniform stored strain can be assumed to be directly related to the strain rate because of the static contributions of SIM as tool velocity changes. The decrease

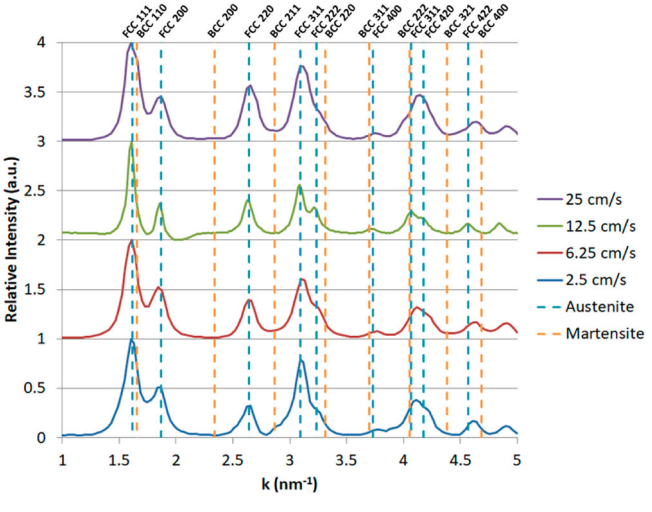

Figure 6. PASAD data plot for the 4 different tool velocities of the linear plane-strain machined chips. The only sample with identifiable amount of SIM is the 2.5 cms^{-1} as noted by the increase in the α'-phase BCC {211} peak.

in the non-uniform stored strain observed with the 25 cms^{-1} tool velocity is consistent with XRD results indicating a strain relief mechanism occurring at this strain rate. The 2.5 cms^{-1} tool velocity exhibits distinguishable peaks for the γ- and α'-phase in the PASAD line profile resulting from a larger SIM volume fraction, such as the α'-phase BCC {211} peak. The PASAD analysis is qualitatively consistent with and confirms our XRD-MVF and VSM-MVF measurement results where there is a significant increase in SIM volume fraction for the chips produced with the 2.5 cms^{-1} tool velocity relative to the other tool velocities. In combination these results suggest a change in the mechanisms activated in response to the severe plastic deformation processing for the regime of strain rates below 2×10^2 s^{-1} and for higher strain rates up to 2×10^3 s^{-1}. For the latter high strain rates in excess of 2×10^2 s^{-1}, the combined effects of adiabatic heating and mechanical stabilisation of the austenite are suppressing the SIM formation and directly affect the resulting grain morphology.

3.3. Geometric dynamic recrystallization at high strain rates

PED-ACOM analysis was performed on the 25 and 12.5 cms^{-1} tool velocity conditions to develop an understanding of morphological changes as the strain rate

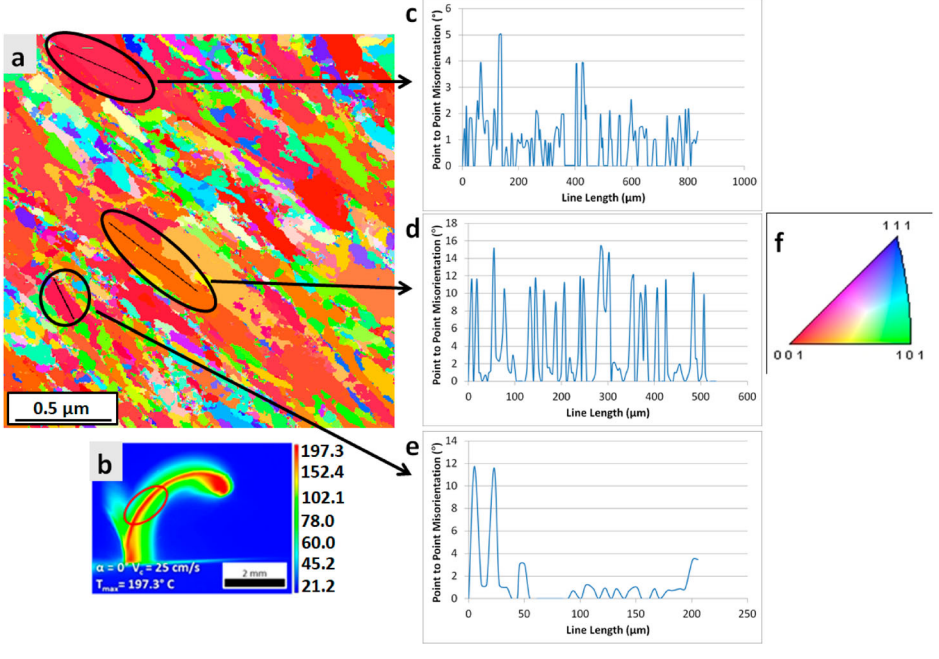

Figure 7. PED-ACOM representation of the (a) 25 cms^{-1} tool velocity condition showing the point-to-point disorientation of various grains in the chip material (c) to (e) along with the (f) IPF map legend. (b) shows an associated IR-thermography still frame. For the 25 cms^{-1} tool velocity condition some grains developed remarkably high point-to-point disorientation (e.g. d), while other grains are nearly strain-free (e.g. e), indicating geometric dynamic recrystallization has occurred.

is increased. Figures 7 and 8 show the inverse pole figure maps for the two chip conditions. Both conditions reveal a grain structure with an irregular shape and grain boundaries exhibiting roughness as a result of the linear plane strain machining. Irregular grain shape is defined here as a grain not possessing a clear shape with any lines of symmetry; an irregular grain shape is expected for a microstructure that undergoes shearing deformation. With an increase in the tool velocity, the grains within the material shifted from a high probability of irregular shaped grains to a high probability of elongated grains, which is presumed to be directly related to the increase in the strain rate. By measuring the point-to-point disorientation, the non-uniform stored strain of the grain interiors can be assessed. The disorientation metrics for the 25 cms^{-1} tool velocity condition reveal a high amount of intragranular strain with a well-developed dislocation sub-cell network. The grains typically exhibit relatively high intragranular point-to-point disorientations with some disorientations exceeding 10 ° (Figure 7c to d); however, it is important to note that some of the grains will show a nearly strain-free state with disorientation ranges from 0 ° to 1 ° (Figure 7e). Meanwhile, for the 12.5 cms^{-1} tool velocity, intragranular point-to-point disorientations remain small where the typical disorientation ranges from 1 ° to 2 ° and very rarely exceed 5 ° (Figure 8c to e). The accuracy of the orientation indexing of the PED-ACOM orientations is limited to ± 0.5 °

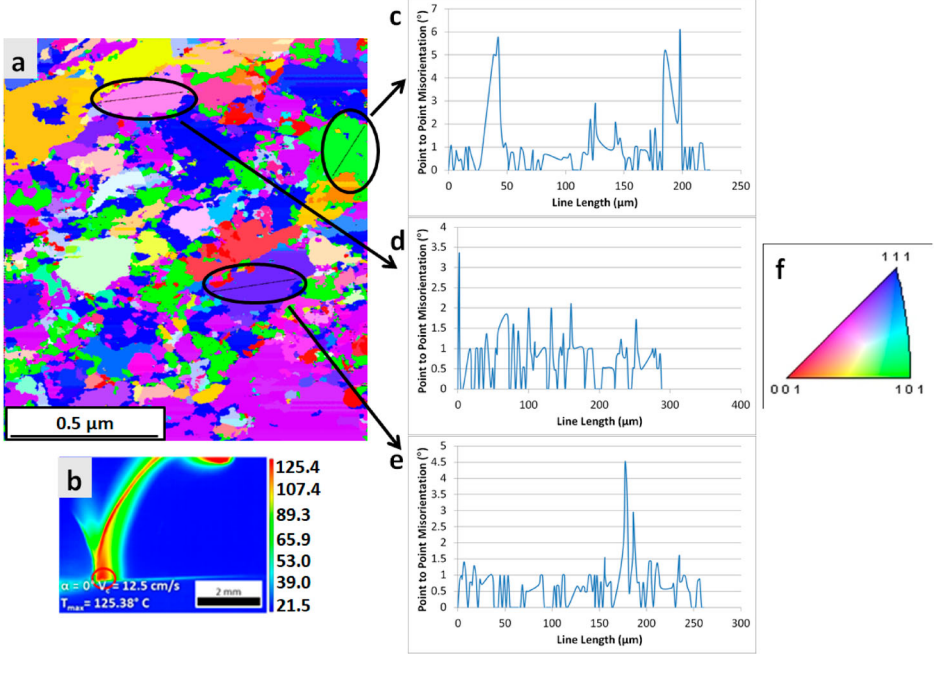

Figure 8. PED-ACOM representation of the (a) 12.5 cms^{-1} tool velocity condition showing the point-to-point disorientation of various grains in the chip material (c) to (e), along with the (f) IPF map legend. (b) displays an associated IR-thermography still frame.

by the angular step increments of the computed reciprocal lattice templates; thus, the disorientation metrics reveal that the differences in the intragranular volumes regarding internal non-uniform strain storage as a direct result of the increase in strain rate is statistically significant.

When the material is deformed during formation of a chip by linear plane-strain machining, the imparted shear strain and strain rate introduce a high defect density leading to the formation of sub-grain cell dislocation networks. The high defect density will lead to increased probability of intragranular slip by dislocations leading to grain elongation along the externally imposed stress axis, which is clearly observed in Figure 7a (25 cms^{-1} tool velocity condition). It is important to note that 316L austenitic stainless steel is considered a medium stacking fault energy material ($\approx$ 50 mJ/m^2 [54]) where twinning is an important deformation mode. However, previous studies have shown that both temperature and grain size have a significant effect on the ability to twin. The stacking fault energy has a positive monotonic function of temperature; when the temperature of the metal increases, the stacking fault energy will also increase. With a higher stacking fault energy, the critical stress required for twin initiation will increase [55]. It has been shown for FCC metals and alloys that the critical stress required for twin initiation increases as grain size decreases, until a critical nanocrystalline grain size is attained, typically between 10 and 100 nm, when an inverse grain size related effect is observed [56]. Based on these two factors, which inhibit twin formation, it is hypothesised that grain refinement is initially primarily controlled by sub-grain rotation [57] and strain-induced twin formation [58], where sub-grain rotation is the dominant grain refinement mechanism in severe plastically deformed materials. After a large strain is imparted, a high density of geometrically necessary dislocations form and rearrange to form into dislocation cells to reduce the total strain energy of the system. As plastic deformation and straining continues, an increasing misorientation develops between the dislocation cells to establish sub-grains. Further deformation permits additional rotation of neighbouring sub-grains relative to each other, until high-angle grain boundaries form, and the size of the original grain has been refined. Once a strain rate in excess of 2×10^2 s^{-1} is achieved during linear plane-strain machining, the combination of grain size reduction and the increase in stacking fault energy through the adiabatic heating of the chip will raise the critical stress required for twin initiation. This renders a change in the primary deformation mode for grain refinement from sub-grain rotation through dislocation pile-up and strain-induced twin formation to dislocation slip resulting in grain elongation.

Within the elongated grains formed as a result of the high strain rate of the 25 cms^{-1} tool velocity ($\approx 2 \times 10^3$ s^{-1}), there are two types of grain morphologies observed: a highly strained grain (Figure 7c) and a nearly strain-free grain (Figure 7d). The highly strained grain is characteristically identified with an elongated morphology, a high density of large intragranular point-to-point

disorientations, and a serrated grain boundary on the scale of the sub-grain dislocation cell facets; meanwhile, the strain-free grain is characterised by an aspect ratio closer to an equiaxed condition, a high density of very small intragranular point-to-point disorientations, and grain boundaries with smaller scale serrations. The latter shares morphological characteristics of those reported for geometric dynamic recrystallization (GDRX), which has been observed previously in Al-Mg alloys [59]. Previous reports of GDRX have been observed during hot rolling or friction welding associated thermo-mechanical processes, where temperatures in excess of 900 °C have been reported [60]. The serrated grain boundaries are the result of pinning and migration induced by the sub-grain boundary formation. As the strain rate increases, the grains become increasingly elongated until the grain thickness is about twice the sub-grain diameter. At this critical grain thickness, the magnitudes of the serrations at the grain boundaries are comparable to the grain width and can connect with one-another across the grain cross-section. The grain boundaries with defects containing opposite signs will annihilate, thereby reducing the excess defect energy, and effectively inducing a 'pinch off' event that produces two new strain-free grains [59]. Evidence consistent with this phenomenon of GDRX is clearly observed for the microstructures that are attained for the SPD in linear plane strain machining with the 25 cms^{1} tool velocity. Here some grains are still highly elongated and internally strained (Figure 7d), while other grains have undergone the process of GDRX and exhibit a smaller aspect ratio and strain-free grain interior (Figure 7e). This recrystallization mechanism is consistent with the XRD data where, in comparison to the lower tool velocity processing conditions, a drop-off in non-uniform micro-strain is observed as tool velocity is increased to 25 cms^{-1}, and a mix of highly strained and strain-free grains present in the microstructure.

The change in microstructural accommodation mechanism for the lower strain rate condition SPD processing at 2×10^2 s^{-1} also explains the softening and apparent inverse Hall-Petch relationship. The Vickers microhardness values are attributed by $\approx$ 20% to grain size strengthening and $\approx$ 80% to other strengthening mechanisms, where the primary contribution is from the SIM. For the 2.5 cms^{-1} tool velocity condition, the significantly larger volume fraction of SIM translates into increased hardness as compared to the higher tool velocity conditions. For the higher tool velocities, the SIM volume fraction is approximately the same, but the hardness continues to drop as function of increasing strain rate. Once the microstructural mechanism changes when the strain rate exceeds 2×10^2 s^{-1}, the recrystallization mechanism of GDRX clearly explains the grain softening. The grains will elongate until they are about twice the sub-grain diameter and then tend to split into new grains of refined size. When the original grain splits, the dislocation density is significantly reduced as dislocation segments of opposite signs annihilate, resulting in a reduction of the stored strain. The combination of reduction in SIM and

non-uniform strain along with minimal dislocation pile-ups due to the dislocation slip being the primary deformation mode therefore results in continued grain softening as strain rate increases.

3.4. Identification of the active dynamic recrystallization process

There are three different types of dynamic recrystallization, namely, discontinuous dynamic recrystallization (DDRX), continuous dynamic recrystallization (CDRX), and GDRX. DDRX is conventionally known as dynamic recrystallization (DRX) and typically has been observed in low to medium SFE materials at high temperatures ($T > 0.5\ T_m$). Because of the lower SFE, it is energetically more favourable for wider stacking faults to form via unit dislocation dissociation. The glide of dissociated dislocation configuration reduces the likelihood for cross-slip and climb related annihilation of opposite sign unit dislocations. As a result, sub-grain structure formation by dynamic recovery (DRV) becomes more difficult during deformation. Eventually, the accumulation of dislocations will lead to local gradients in dislocation density that are large enough to allow formation of new grains through a distinct nucleation and growth stage. DDRX is primarily identified by strain induced bulging of the original grain boundaries that lead to a necklace structure of fine equiaxed recrystallized grains along the grain boundaries [61]. Meanwhile, neither CDRX or GDRX have distinguishable nucleation and growth stages during the recrystallization process due to rapid DRV [59,62,63]. Because of the rapid DRV in CDRX, dislocations arrange in a cell structure that progressively rotates sub-grains into recrystallized grains through either a homogeneous increase in disorientation angle or by the formation of micro-shear bands [64–66]. In previous studies CDRX has only been observed by processing the material through SPD techniques, such as ECAP, HPT, multi-directional forging, and accumulative roll bonding [67]. At low temperatures ($T < 0.5\ T_m$), CDRX typically occurs in metals and alloys independent of their SFE [68,69], while only high SFE materials have been observed to exhibit CRDX at higher temperatures ($T > 0.5\ T_m$) [70,71]. On the other hand, GDRX produces a new grain structure resulting from the change in grain geometry during deformation. The GDRX mechanism has been described as the formation of equiaxed grains during single directional hot deformation by the migration of high-angle grain boundaries (HAGBs) to form serrations, thinning of the grain thickness, and the impingement of serrated HAGBs when the dimensions of the grain cross-sections approach critical values of about two times the sub-grain size, which causes the original grain to 'pinch-off' into two separate recrystallized grains [59]. Previous studies have only observed GDRX in aluminum and its alloys (i.e. high SFE materials) at high temperatures, but this phenomenon can theoretically lead to grain refinement in FCC, BCC, or HCP metals [72]. Due to the limited studies of GDRX, it is unclear if medium SFE materials are capable of rapid DRV, which would allow GDRX to occur.

Thus far, the studies of GDRX have been limited to high SFE materials while austenitic stainless steel has never been linked to this type of dynamic recrystallization. Austenitic stainless steels have a range of SFEs that depend on the alloying additions; some examples include low SFEs such as 301LN (≈ 12 mJ/m^2 [73]) and 304 (≈ 21 mJ/m^2 [74]) or a medium SFE of 316L (≈ 50 mJ/m^2 [54]). Rapid DRV is a key element for GDRX and would be expected to be more difficult in the lower SFE materials, such as 301LN and 304 austenitic stainless steels, than in 316L with a medium SFE. The plastic deformation of the medium SFE of 316L is much less prone to mechanical twinning than that of 301LN and permits development of characteristic dislocation cell structures at room temperature for sufficiently high strain and straining rates. We posit that aside from SFE of an alloy it is important to consider additional factors, such as the combination of grain size, temperature, strain, and strain rate, in attempts to assess whether rapid DRV, and concurrently GDRX, can occur in a material.

Even though there are several similarities between the phenomena of CDRX and GDRX, due to both DRX processes relying on DRV, several key distinguishing features can be identified. CDRX can be characterised by the following: (i) the average disorientations are increasing with strain [75,76]; (ii) the transformation of low angle grain boundaries into HAGBs is observed by the progressive lattice rotation near grain boundaries or by the formation of micro-shear bands at large strains [77]; (iii) the average grain size decreases with deformation and reaches a steady-state value at large strains, while some stable original grains remain unchanged even at large strains [70,78]; (iv) a strong crystallographic texture from inhomogeneous lattice rotation constraints between the grain boundary and grain interior [79]. Meanwhile, GDRX specific features can be identified as follows: (i) sub-grains are formed after a critical deformation, first near original HAGBs, and the sub-grains remain approximately equiaxed and constant in size [80]; (ii) the recrystallization texture during GDRX remains largely unchanged [81]; (iii) when solute drag and/or particle pinning are involved, the critical strain for sub-grain formation and the HAGB fraction increases, but the steady state sub-grain size decreases, which also means large deformation is required to complete GDRX [82].

One of the key distinctions for DDRX is possessing distinct nucleation and growth stages where DRV is not a dominant process. DRV will lead to annihilation of dislocations with opposite signs and dislocations with the same sign will rearrange themselves into ordered arrays where the individual contribution to the stored energy is reduced by the overlapping of their strain fields during deformation. For higher SFE materials, dissociation of the perfect dislocation into two partial dislocations is more difficult and rearrangement of the mobile perfect dislocation takes place more readily through glide, climb, and cross-slip permitting rapid DRV to occur. Therefore, dislocations will arrange into a sub-cell network that eventually will develop into sub-grains leading to either CDRX or GDRX during rapid DRV. If DRV is not rapid enough, the dislocation

density will increase to a critical density at which the difference in local dislocation density on both sides of a grain boundary will constitute a driving force large enough to initiate recrystallization [83]. Once recrystallized, the grain boundary migration will occur very quickly leading to a necklace structure of refined equiaxed grains along the grain boundaries.

In the linear plane-strain machined chips, we simultaneously observe elongated grains with high strain (i.e. deformed) and strain-free newly recrystallized equiaxed grains (Figure 5a to c and Figure 7) in the microstructure. This suggests that there are no distinct nucleation and growth stages during deformation. The elongated grain morphology strongly suggests that slip is the primary deformation mechanism and rapid DRV is occurring. Therefore, DDRX can be ruled out as the dominant microstructural process. There appears to be a change in the type of DRX occurring around a strain rate of 4×10^2 s^{-1} (Figure 5). Above a strain rate of 4×10^2 s^{-1}, there is little change in texture (Figure 5e to g), significant grain elongation and thinning of the grain cross-sections (Figure 5a to c), no distinct nucleation and growth stage, and only a small deviation about the mean grain size, suggesting a relatively homogenous grain size distribution (Table 2). Additionally, grain boundary serrations appear along the elongated grains. Taken individually and in combination these features are consistent with GDRX being the primary dynamic recrystallization mechanism at these strain rates. On the other hand, below a strain rate of 4×10^2 s^{-1}, a strong texture (Figure 5h) with a larger deviation about the mean grain size (Table 2). The larger deviation about the mean grain size indicates that some grains did not further refine even though a large strain is present. The heterogenous grain size distribution and strong texture are consistent with the prototypical description of a microstructure refined by CDRX. It therefore appears reasonable to conclude that the primary recrystallization mechanism is CDRX until the strain rate reaches a critical value, here slightly below 4×10^2 s^{-1}, when it changes to GDRX as the dominant and primary recrystallization mechanism.

4. Conclusions

A novel single-pass surface-severe-plastic-deformation (SSPD) technique, linear plane-strain machining, has been applied to 316L austenitic stainless steel at room temperature and imparted shear strains up to 2.2 while processing at strain rates between 2×10^2 s^{-1}–2×10^3 s^{-1} that led to significant grain size refinement and mechanical strength improvement in the resultant chip. The mechanical property and microstructural changes were monitored through a combination of hardness measurements, VSM measurements, XRD, TEM, and IR-thermography. The processing-microstructure-property relationships are developed to understand the underlying mechanisms from the linear plane-strain machining, and can be summarised as follows:

(1) The chips exhibit an observed change in the microstructural mechanisms responsible for the grain morphology and scale changes occurring between the strain rates of 2×10^2 s^{-1}–4×10^2 s^{-1}. For strain rate below 2×10^2 s^{-1} significantly more SIM is observed in the SSPD processed 316L microstructure with a bimodal grain size distribution. In contrast, for strain rates above 4×10^2 s^{-1}, a reduced amount of SIM in a microstructure with a unimodal grain size distribution resulted. These characteristic differences are attributed to the combined effects of adiabatic heating, mechanical stabilisation of the austenite, and a change in the grain refinement mechanism.
(2) The chips are also observed to form a gradient microstructure where a maximum amount of SIM is formed at the surface with less SIM formed near the centre.
(3) The adiabatic heating of the chips increased the stacking fault energy, which in combination with the significant grain refinement suppressed strain-induced twinning. As a result, the thermo-mechanically processed chip microstructure clearly shows the deformation mode changes from sub-grain rotation through dislocation pile-up and strain-induced twin formation to dislocation slip. As the strain rate is increased from 4×10^2 s^{-1}–2×10^3 s^{-1}, the grain morphology shifted from a distribution of grains comprising a large fraction of irregular shaped grains to one dominated by self-similar elongated shape grains with a microstructure characterised by an increased intra-granular dislocation density forming sub-grain networks, and serrated grain boundaries. Once the thickness of the elongated grains is reduced to approximately twice the sub-grain diameter, the grain boundary segments containing defects with opposite signs will annihilate each other, resulting in splitting the elongated grains into two strain-free grains.
(4) The combination of reduction in SIM and non-uniform intragranular strain along with grain refinement as function of increasing strain rate led to an observed Hall-Petch relationship with a negative strengthening coefficient of -0.08 MPa $m^{1/2}$, i.e. inverse Hall-Petch behaviour with softening as the grain scale refines. It can be concluded that geometric dynamic recrystallization is observed in 316L austenitic stainless steel after room temperature linear plane-strain machining, i.e. after high-strain-rate SPD.

Acknowledgements

The Nuclear Regulatory Commission (NRC-38-09-935), the National Science Foundation (NSF CMMI #1635926) and the Materials Micro-Characterization Laboratory, Department of Mechanical Engineering and Materials Science, of the Swanson School of Engineering at the University of Pittsburgh are acknowledged for their financial and infrastructure support.

Disclosure statement

No potential conflict of interest was reported by the author(s).

Funding

This work was supported by Division of Civil, Mechanical and Manufacturing Innovation: [Grant Number 1635926]; U.S. Nuclear Regulatory Commission: [Grant Number NRC-38-09-935].

ORCID

Yaakov Idell http://orcid.org/0000-0002-4557-8653

References

[1] M.F. McGuire, *Stainless Steels for Design Engineers*, Asm International, Materials Park, OH, 2008.

[2] K. Spencer, M. Véron, K. Yu-Zhang and J.D. Embury, *The strain induced martensite transformation in austenitic stainless steels: Part 1–influence of temperature and strain history*. Mater. Sci. Technol 25 (2009), pp. 7–17.

[3] C. Ye, A. Telang, A.S. Gill, S. Suslov, Y. Idell, K. Zweiacker, J.M.K. Wiezorek, Z. Zhou, D. Qian, S.R. Mannava and V.K. Vasudevan, *Gradient nanostructure and residual stresses induced by ultrasonic nano-crystal surface modification in 304 austenitic stainless steel for high strength and high ductility*. Mater. Sci. Eng. A 613 (2014). doi:10.1016/j.msea.2014.06.114.

[4] M. Eskandari, A. Najafizadeh and A. Kermanpur, *Effect of strain-induced martensite on the formation of nanocrystalline 316L stainless steel after cold rolling and annealing*. Mater. Sci. Eng. A 519 (2009), pp. 46–50. doi:10.1016/j.msea.2009.04.038.

[5] A.F. Padilha, R.L. Plaut and P.R. Rios, *Annealing of cold-worked austenitic stainless steels*. ISIJ Int. 43 (2003), pp. 135–143. doi:10.2355/isijinternational.43.135.

[6] T. Angel, *Formation of martensite in austenitic stainless steels*. J. Iron Steel Inst 177 (1954), pp. 165–174.

[7] G.V. Kurdyumov and O.P. Maksimova, *Kinetics of the transformation of austenite into martensite at low temperatures*. Dokl. Akad. Nauk SSSR 61 (1948), pp. 83–86.

[8] V.M. Segal, V.I. Reznikov, A.E. Dobryshevshiy, and V.I. Kopylov, *Plastic working of metals by simple shear*. Russ. Metall 1 (1981), pp. 99–105.

[9] R.Z. Valiev, I.V. Alexandrov, Y.T. Zhu and T.C. Lowe, *Paradox of strength and ductility in metals processed by severe plastic deformation*. J. Mater. Res 17 (2002), pp. 5–8. doi:10.1557/JMR.2002.0002.

[10] N.A. Smirnova, V.I. Levit, V.I. Pilyugin, R.I. Kuznetsov, L.S. Davydova and V.A. Sazonova, *Evolution of structure of FCC single crystals during strong plastic deformation*. Phys. Met. Met 61 (1986), pp. 127–134.

[11] J. Languillaume, F. Chmelik, G. Kapelski, F. Bordeaux, A.A. Nazarov, G. Canova, C. Esling, R.Z. Valiev and B. Baudelet, *Microstructures and hardness of ultrafine-grained Ni3Al*. Acta Metall. Mater 41 (1993), pp. 2953–2962. doi:10.1016/0956-7151(93)90110-E.

[12] R.K. Islamgaliev, F. Chmelik, I.F. Gibadullin, W. Biegel and R.Z. Valiev, *The nanocrystalline structure formation in germanium subjected to severe plastic deformation*. Nanostructured Mater 4 (1994), pp. 387–395. doi:10.1016/0965-9773(94)90109-0.

[13] X.H. Chen, J. Lu, L. Lu and K. Lu, *Tensile properties of a nanocrystalline 316L austenitic stainless steel*. Scr. Mater 52 (2005), pp. 1039–1044. doi:10.1016/j.scriptamat.2005.01.023.

[14] Z. Pakieła, M. Suś-Ryszkowska, A. Drużycka-Wiencek, K. Sikorski and K.J. Kurzydłowski, *Microstructure and properties of nano-metals obtained by severe plastic deformation*. Inżynieria Mater 25 (2004), pp. 407–410.

[15] R.Z. Valiev, N.A. Krasilnikov and N.K. Tsenev, *Plastic deformation of alloys with sub-micron-grained structure*. Mater. Sci. Eng. A 137 (1991), pp. 35–40. doi:10.1016/0921-5093(91)90316-F.

[16] R.Z. Valiev, N.K. Tsenev, T.G. *Hot Deformation of Aluminum Alloys* (T.G. Langdon, H.D. Merchant, J.G. Morris, M.A. Zaidi, eds.), The Mines, Metals, and Materials Society, Warrendale, PA, 1991, 319.

[17] Y. Idell, G. Facco, A. Kulovits, M.R. Shankar and J.M.K. Wiezorek, *Strengthening of austenitic stainless steel by formation of nanocrystalline γ-phase through severe plastic deformation during two-dimensional linear plane-strain machining*. Scr. Mater 68 (2013), pp. 667–670. doi:10.1016/j.scriptamat.2013.01.025.

[18] S. Swaminathan, M.R. Shankar, B.C. Rao, W.D. Compton, S. Chandrasekar, A.H. King and K.P. Trumble, *Severe plastic deformation (SPD) and nanostructured materials by machining*. J. Mater. Sci 42 (2007), pp. 1529–1541. doi:10.1007/s10853-006-0745-9.

[19] B.L. Juneja, *Fundamentals of Metal Cutting and Machine Tools*, New Age International, New Dehli, India, 2003.

[20] S. Swaminathan, M.R. Shankar, S. Lee, J. Hwang, A.H. King, R.F. Kezar, B.C. Rao, T.L. Brown, S. Chandrasekar and W.D. Compton, *Large strain deformation and ultra-fine grained materials by machining*. Mater. Sci. Eng. A 410 (2005), pp. 358–363. doi:10.1016/j.msea.2005.08.139.

[21] J.M.K. Wiezorek, G. Facco, Y. Idell, A. Kulovits, and M.R. Shankar, *Nano-structuring of 316L type steel by severe plastic deformation processing using two-dimensional linear plane strain machining*. Mater. Sci. Forum 783–786 (2014), pp. 2720–2725. www.scientific.net/MSF.783-786.2720.

[22] J. Portillo, E.F. Rauch, S. Nicolopoulos, M. Gemmi, and D. Bultreys, *Precession electron diffraction assisted orientation mapping in the transmission electron microscope*, in *Mater. Sci. Forum*, Trans Tech Publications Ltd, Zurich, Switzerland, 2010. pp. 1–7.

[23] M. Wojdyr, *Fityk: a general-purpose peak fitting program*. J. Appl. Crystallogr 43 (2010), pp. 1126–1128. doi:10.1107/S0021889810030499.

[24] M.E. Merchant, *Mechanics of the metal cutting process. I. Orthogonal cutting and a type 2 chip*. J. Appl. Phys. 16 (1945), pp. 267–275. doi:10.1063/1.1707586.

[25] M.C. Shaw and J.O. Cookson, *Metal Cutting Principles*, Oxford university press, New York, 2005.

[26] H. Ueno, K. Kakihata, Y. Kaneko, S. Hashimoto and A. Vinogradov, *Nanostructurization assisted by twinning during equal channel angular pressing of metastable 316L stainless steel*. J. Mater. Sci 46 (2011), pp. 4276–4283. doi:10.1007/s10853-011-5303-4.

[27] A. Sarkar, A. Bhowmik and S. Suwas, *Microstructural characterization of ultrafine-grain interstitial-free steel by X-ray diffraction line profile analysis*. Appl. Phys. A 94 (2009), pp. 943–948. doi:10.1007/s00339-008-4870-y.

[28] B.P. Kashyap and K. Tangri, *Hall-Petch relationship and substructural evolution in boron containing type 316L stainless steel*. Acta Mater. 45 (1997), pp. 2383–2395. doi:10.1016/S1359-6454(96)00341-2.

[29] J.S.C. Jang and C.C. Koch, *The Hall-Petch relationship in nanocrystalline iron produced by ball milling*. Scr. Metall. Mater 24 (1990), pp. 1599–1604. doi:10.1016/0956-716X(90)90439-N.
[30] M. Zhao and Q. Jiang, *Reverse hall-petch relationship of metals in nanometer size*, in *2006 IEEE Conf. Emerg. Technol., Singapore*, IEEE, 2006. pp. 472–474.
[31] T.G. Nieh and J. Wadsworth, *Hall-Petch relation in nanocrystalline solids*. Scr. Metall. Mater 25 (1991), pp. 955–958. doi:10.1016/0956-716X(91)90256-Z.
[32] B. Cai, Q.P. Kong, L. Lu and K. Lu, *Interface controlled diffusional creep of nanocrystalline pure copper*. Scr. Mater. 41 (1999), pp. 755–759.
[33] A.H. Chokshi, A. Rosen, J. Karch and H. Gleiter, *On the validity of the Hall-Petch relationship in nanocrystalline materials*. Scr. Metall 23 (1989), pp. 1679–1683. doi:10.1016/0036-9748(89)90342-6.
[34] H. Hahn and K.A. Padmanabhan, *A model for the deformation of nanocrystalline materials*. Philos. Mag. B 76 (1997), pp. 559–571. doi:10.1080/01418639708241122.
[35] H. Van Swygenhoven, M. Spaczer and A. Caro, *Microscopic description of plasticity in computer generated metallic nanophase samples: a comparison between Cu and Ni*. Acta Mater. 47 (1999), pp. 3117–3126. doi:10.1016/S1359-6454(99)00109-3.
[36] G. Palumbo, U. Erb and K.T. Aust, *Triple line disclination effects on the mechanical behaviour of materials*. Scr. Metall. Mater 24 (1990), pp. 2347–2350. doi:10.1016/0956-716X(90)90091-T.
[37] J.B. Nelson and D.P. Riley, *An experimental investigation of extrapolation methods in the derivation of accurate unit-cell dimensions of crystals*. Proc. Phys. Soc 57 (1945), pp. 160–177. doi:10.1088/0959-5309/57/3/302.
[38] B.D. Cullity and S.R. Stock, *Elements of X-Ray Diffraction*, 3rd ed., Prentice Hall, Upper Saddle River, 2001.
[39] G.K. Williamson and W.H. Hall, *X-ray line broadening from filed aluminium and wolfram*. Acta Met 1 (1953), pp. 22–31. doi:10.1016/0001-6160(53)90006-6.
[40] A.L. Patterson, *The Scherrer formula for X-ray particle size determination*. Phys. Rev 56 (1939), pp. 978–982. doi:10.1103/PhysRev.56.978.
[41] J. Speer, D.K. Matlock, B.C. De Cooman and J.G. Schroth, *Carbon partitioning into austenite after martensite transformation*. Acta Mater. 51 (2003), pp. 2611–2622. doi:10.1016/S1359-6454(03)00059-4.
[42] H.C. Fiedler, *The effect of deformation on the martensitic transformation in austenitic stainless steels*. Trans. ASM 47 (1955), pp. 267–290.
[43] E.S. Machlin and M. Cohen, *Burst phenomenon in the martensitic transformation*. JOM 3 (1951), pp. 746–754. doi:10.1007/BF03397387.
[44] J.F. Breedis and W.D. Robertson, *Martensitic transformation and plastic deformation in iron alloy single crystals*. Acta Metall. 11 (1963), pp. 547–559. doi:10.1016/0001-6160(63)90089-0.
[45] J.R. Strife, M.J. Carr and G.S. Ansell, *The effect of austenite prestrain above the M d temperature on the martensitic transformation in Fe-Ni-Cr-C alloys*. Metall. Trans. A 8 (1977), pp. 1471–1484. doi:10.1007/BF02642861.
[46] H.X. Gao and L.-M. Peng, *Parameterization of the temperature dependence of the Debye–waller factors*. Acta Crystallogr. Sect. A Found. Crystallogr 55 (1999), pp. 926–932. doi:10.1107/S0108767399005176.
[47] T. Hahn, U. Shmueli, and J.C.W. Arthur, *International Tables for Crystallography*, Reidel Dordrecht, Berlin, Germany1983.
[48] S. Abolghasem, S. Basu, S. Shekhar, J. Cai and M.R. Shankar, *Mapping subgrain sizes resulting from severe simple shear deformation*. Acta Mater. 60 (2012), pp. 376–386. doi:10.1016/j.actamat.2011.09.055.

[49] D. Umbrello, R. M'saoubi and J.C. Outeiro, *The influence of Johnson–cook material constants on finite element simulation of machining of AISI 316L steel*. Int. J. Mach. Tools Manuf 47 (2007), pp. 462–470. doi:10.1016/j.ijmachtools.2006.06.006.
[50] G.R. Johnson, *A constitutive model and data for materials subjected to large strains, high strain rates, and high temperatures*. Proc. 7th Inf. Sympo. Ballist. 1 (1983), pp. 541–547.
[51] A.H. Adibi-Sedeh, V. Madhavan and B. Bahr, *Extension of Oxley's analysis of machining to use different material models*. J. Manuf. Sci. Eng 125 (2003), pp. 656–666. doi:10.1115/1.1617287.
[52] H. Chandrasekaran, R. M'saoubi and H. Chazal, *Modelling of material flow stress in chip formation process from orthogonal milling and split Hopkinson bar tests*. Mach. Sci. Technol 9 (2005), pp. 131–145. doi:10.1081/MST-200051380.
[53] C. Gammer, C. Mangler, C. Rentenberger and H.P. Karnthaler, *Quantitative local profile analysis of nanomaterials by electron diffraction*. Scr. Mater 63 (2010), pp. 312–315. doi:10.1016/j.scriptamat.2010.04.019.
[54] H.F.G. de Abreu, S.S. de Carvalho, P. de Lima Neto, R.P. dos Santos, V.N. Freire, P.M.d.O. Silva and S.S.M. Tavares, *Deformation induced martensite in an AISI 301LN stainless steel: characterization and influence on pitting corrosion resistance*. Mater. Res 10 (2007), pp. 359–366. doi:10.1590/S1516-1439200700040.
[55] X. Wu, X. Pan, J.C. Mabon, M. Li and J.F. Stubbins, *The role of deformation mechanisms in flow localization of 316L stainless steel*. J. Nucl. Mater. 356 (2006), pp. 70–77. doi:10.1016/j.jnucmat.2006.05.047.
[56] Y.T. Zhu, X.Z. Liao, X.L. Wu and J. Narayan, *Grain size effect on deformation twinning and detwinning*. J. Mater. Sci 48 (2013), pp. 4467–4475. doi:10.1007/s10853-013-7140-0.
[57] A. Mishra, B.K. Kad, F. Gregori and M.A. Meyers, *Microstructural evolution in copper subjected to severe plastic deformation: experiments and analysis*. Acta Mater. 55 (2007), pp. 13–28. doi:10.1016/j.actamat.2006.07.008.
[58] N.R. Tao and K. Lu, *Nanoscale structural refinement via deformation twinning in face-centered cubic metals*. Scr. Mater 60 (2009), pp. 1039–1043. doi:10.1016/j.scriptamat.2009.02.008.
[59] A. Rollett, F.J. Humphreys and G.S. Rohrer, *Recrystallization and Related Annealing Phenomena*, 3rd ed., Elsevier, Cambride, 2017.
[60] J. Junior, A. Moreira and O. Balancin, *Prediction of steel flow stresses under hot working conditions*. Mater. Res. 8 (2005), pp. 309–315. doi:10.1590/S1516-14392005000300015.
[61] D. Ponge and G. Gottstein, *Necklace formation during dynamic recrystallization: mechanisms and impact on flow behavior*. Acta Mater. 46 (1998), pp. 69–80. doi:10.1016/S1359-6454(97)00233-4.
[62] S. Gourdet and F. Montheillet, *An experimental study of the recrystallization mechanism during hot deformation of aluminium*. Mater. Sci. Eng. A 283 (2000), pp. 274–288. doi:10.1016/S0921-5093(00)00733-4.
[63] C. Perdrix, M.Y. Perrin, and F. Montheillet, *Mechanical Behavior and structure development of aluminum during Hot deformation With large Amplitude*. Mem. Etud. Sci. Rev. Met 78 (1981), pp. 309–320.
[64] S. White, *A Discussion on natural strain and geological structure-The effects of strain on the microstructures, fabrics, and deformation mechanisms in quartzites*. Philos. Trans. R. Soc. London. Ser. A, Math. Phys. Sci. 283 (1976), pp. 69–86. doi:10.1098/rsta.1976.0070.
[65] S.E. Ion, F.J. Humphreys and S.H. White, *Dynamic recrystallisation and the development of microstructure during the high temperature deformation of magnesium*. Acta Metall. 30 (1982), pp. 1909–1919. doi:10.1016/0001-6160(82)90031-1.

[66] T. Sakai, A. Belyakov and H. Miura, *Ultrafine grain formation in ferritic stainless steel during severe plastic deformation*. Metall. Mater. Trans. A 39 (2008), pp. 2206–2214. doi:10.1007/s11661-008-9556-8.

[67] T. Sakai, A. Belyakov, R. Kaibyshev, H. Miura and J.J. Jonas, *Dynamic and post-dynamic recrystallization under hot, cold and severe plastic deformation conditions*. Prog. Mater. Sci 60 (2014), pp. 130–207. doi:10.1016/j.pmatsci.2013.09.002.

[68] F. Montheillet and J.-P. Thomas, *Dynamic recrystallization of low stacking fault energy metals*, in *Met. Mater. with High Struct. Effic*, Senkov O., Miracle D., Firstov S., eds., Springer, New York, NY, 2004. pp. 357–368.

[69] Z. Yanushkevich, A. Belyakov and R. Kaibyshev, *Microstructural evolution of a 304-type austenitic stainless steel during rolling at temperatures of 773–1273 K*. Acta Mater. 82 (2015), pp. 244–254. doi:10.1016/j.actamat.2014.09.023.

[70] O. Sitdikov and R. Kaibyshev, *Dynamic recrystallization in pure magnesium*. Mater. Trans 42 (2001), pp. 1928–1937. doi:10.2320/matertrans.42.1928.

[71] H.J. McQueen and W. Blum, *Dynamic recovery: sufficient mechanism in the hot deformation of Al (< 99.99)*. Mater. Sci. Eng. A 290 (2000), pp. 95–107. doi:10.1016/S0921-5093(00)00933-3.

[72] M.E. Kassner and S.R. Barrabes, *New developments in geometric dynamic recrystallization*. Mater. Sci. Eng. A 410 (2005), pp. 152–155. doi:10.1016/j.msea.2005.08.052.

[73] J. Talonen and H. Hänninen, *Formation of shear bands and strain-induced martensite during plastic deformation of metastable austenitic stainless steels*. Acta Mater. 55 (2007), pp. 6108–6118. doi:10.1016/j.actamat.2007.07.015.

[74] L.E. Murr, *Interfacial Phenomena in Metals and Alloys*, Addison Wesley Publishing Company, Reading, MA, 1975.

[75] R. Kaibyshev, K. Shipilova, F. Musin and Y. Motohashi, *Continuous dynamic recrystallization in an Al–Li–Mg–Sc alloy during equal-channel angular extrusion*. Mater. Sci. Eng. A 396 (2005), pp. 341–351. doi:10.1016/j.msea.2005.01.053.

[76] K. Tsuzaki, X. Huang and T. Maki, *Mechanism of dynamic continuous recrystallization during superplastic deformation in a microduplex stainless steel*. Acta Mater. 44 (1996), pp. 4491–4499. doi:10.1016/1359-6454(96)00080-8.

[77] W.C. Liu, D.J. Jensen and J.G. Morris, *Effect of grain orientation on microstructures during hot deformation of AA 3104 aluminium alloy by plane strain compression*. Acta Mater. 49 (2001), pp. 3347–3367. doi:10.1016/S1359-6454(01)00009-X.

[78] X. Yang, H. Miura and T. Sakai, *Dynamic evolution of new grains in magnesium alloy AZ31 during hot deformation*. Mater. Trans 44 (2003), pp. 197–203. doi:10.2320/matertrans.44.197.

[79] L.S. Tóth, Y. Estrin, R. Lapovok and C. Gu, *A model of grain fragmentation based on lattice curvature*. Acta Mater. 58 (2010), pp. 1782–1794. doi:10.1016/j.actamat.2009.11.020.

[80] G.A. Henshall, M.E. Kassner and H.J. McQueen, *Dynamic restoration mechanisms in Al-5.8 At. Pct Mg deformed to large strains in the solute drag regime*. Metall. Trans. A 23 (1992), pp. 881–889. doi:10.1007/BF02675565.

[81] A. Gholinia, F.J. Humphreys and P.B. Prangnell, *Production of ultra-fine grain microstructures in Al–Mg alloys by coventional rolling*. Acta Mater. 50 (2002), pp. 4461–4476. doi:10.1016/S1359-6454(02)00253-7.

[82] H.J. McQueen, O. Knustad, N. Ryum and J.K. Solberg, *Microstructural evolution in Al deformed to strains of 60 at 400 C*. Scr. Metall. 19 (1985), pp. 73–78.

[83] R. Sandström and R. Lagneborg, *A model for hot working occurring by recrystallization*. Acta Metall. 23 (1975), pp. 387–398. doi:10.1016/0001-6160(75)90132-7.